

Insulin receptor activation by proinsulin preserves synapses and vision in retinitis pigmentosa

Alonso Sánchez-Cruz

Centro de Investigaciones Biologicas

Alberto Hernández-Pinto

Centro de Investigaciones Biologicas

Concepción Lillo

Universidad de Salamanca

Carolina Isiegas

Centro de Investigaciones Biologicas

Miguel Marchena

Centro de Investigaciones Biologicas

Ignacio Lizasoain

Universidad Complutense de Madrid Facultad de Medicina

Fátima Bosch

Universitat Autònoma de Barcelona

Pedro de la Villa

Universidad de Alcalá de Henares Facultad de Medicina y Ciencias de la Salud

Catalina Hernández-Sánchez (✉ chemandez@cib.csic.es)

Centro de Investigaciones Biologicas <https://orcid.org/0000-0002-0846-5019>

Enrique J. de la Rosa

Centro de Investigaciones Biologicas

Research article

Keywords: Insulin receptor, pS6, neurodegeneration, synapses, retina

Posted Date: July 14th, 2020

DOI: <https://doi.org/10.21203/rs.3.rs-41130/v1>

License: © ⓘ This work is licensed under a Creative Commons Attribution 4.0 International License.

[Read Full License](#)

Version of Record: A version of this preprint was published at Cell Death & Disease on April 1st, 2022. See the published version at <https://doi.org/10.1038/s41419-022-04839-0>.

Abstract

Background

Synaptic loss, neuronal cell death, and circuit remodeling are common features of central nervous system neurodegenerative disorders. Retinitis pigmentosa, the leading cause of inherited blindness, is a group of retinal dystrophies characterized by photoreceptor cell dysfunction and death. The insulin receptor, a key controller of metabolism, also regulates neuronal survival and synaptic formation, maintenance, and activity. Indeed, deficient insulin receptor signaling has been implicated in several brain neurodegenerative pathologies.

Methods

We employed a gene therapy strategy to enhance insulin receptor signaling in the Pde6b rd10/rd10 mouse model of RP by using recombinant AAV serotype 2/1 viral vectors bearing cDNA from the human proinsulin gene. Insulin receptor expression and signaling were analyzed by PCR and immunostaining. Synaptic connectivity was evaluated by electron microscopy and immunostaining. Proinsulin levels were measured by ELISA. Photoreceptor preservation was assayed by histological analysis and visual function was assessed by electroretinography and optomotor test.

Results

We present evidence linking impaired insulin receptor signaling with retinitis pigmentosa. We found a selective decrease in the levels of the insulin receptor and its downstream effector phospho-S6 in retinal horizontal cell axons in the rd10 mouse model of retinitis pigmentosa, as well as aberrant synapses between rod photoreceptors and the postsynaptic terminals of horizontal and bipolar cells. A gene therapy strategy to induce sustained proinsulin production restored retinal insulin receptor signaling, by increasing S6 phosphorylation, without peripheral metabolic consequences. Moreover, proinsulin preserved photoreceptor synaptic connectivity and prolonged visual function as determined by electroretinography and optomotor tests.

Conclusion

These findings point to a disease-modifying role of insulin receptor and support the therapeutic potential of proinsulin in retinitis pigmentosa.

Background

Neurodegenerative disorders are complex pathological conditions that involve, among other processes, synaptic loss and neuronal cell death leading to deterioration of neuronal structure and function. According to the 2016 Global Burden of Disease report [1], neurodegenerative diseases are the second leading cause of death and a major cause of disability. The development of strategies to cure or at least delay the progression of neurodegenerative diseases has been hindered by their diverse etiology and

complex nature, and by the limited regenerative capacity of neurons. There is thus an urgent need for effective medical interventions. As part of the central nervous system (CNS), the retina shares multiple pathophysiological features with the brain [2]. Despite their diverse etiology, retinal neurodegenerative diseases, like those affecting the brain, are characterized by synaptic failure and neuronal cell death [3]. Retinitis pigmentosa (RP) comprises a group of hereditary retinal neurodegenerative conditions with a complex genetic etiology. To date more than 60 genes and 3,000 mutations have been implicated in RP, and over 300 genes associated with inherited retinal dystrophies (<https://sph.uth.edu/retnet/disease.htm>) have been identified. RP is characterized by primary dysfunction and death of photoreceptor cells followed by reactive gliosis and remodeling of the retinal structure, resulting in vision loss and eventual blindness [3, 4]. RP is categorized as a rare disease (prevalence 1/3,500-4,000), but accounts for most cases of hereditary blindness. Gene therapy would be the ideal definitive treatment, and one such therapy has been recently approved for a related retinal dystrophy [5]. However, the complexity and diversity of the mutations underlying RP necessitate the development of alternative therapeutic approaches, particularly those independent of the causative mutation, as well as palliative treatments. The insulin receptor (INSR), traditionally considered a key peripheral metabolic regulator, is increasingly viewed as an important modulator of neuronal cell survival, and synaptic formation, maintenance, and activity [6–8]. Since initial reports described widespread INSR expression in the CNS, including the retina [9–13], INSR signaling has been implicated in a growing number of CNS functions. In addition to regulating feeding behavior and peripheral metabolism, central INSR signaling is involved in memory formation and cognitive functions [6, 7, 14]. The mechanisms underpinning the non-metabolic actions of INSR are being gradually unraveled. At the neuronal level, INSR is involved in the control of synaptic function, through regulation of neurotransmitter receptor trafficking, and in synapse maintenance and dendritic arbor formation [8, 15]. Downregulation of INSR signaling has been implicated in several neurodegenerative diseases [6], particularly Alzheimer’s disease [16–19], and INSR stimulation proposed as a potential treatment for neurodegenerative disorders [20].

We previously showed that INSR stimulation in the embryonic retina promotes neuronal differentiation and downregulates developmental cell death [21, 22], and that the insulin precursor proinsulin (Pi) can slow RP progression [23–25]. In the present study, we investigated the role of INSR in retinal neurodegeneration and sought to characterize the neuroprotective role of Pi as a putative INSR ligand. We present the first evidence linking impaired INSR signaling with retinal neurodegeneration, and provide insight into the multifaceted neuroprotective role of INSR. We employed a gene therapy strategy to produce sustained increases in systemic Pi levels without peripheral metabolic consequences. Pi treatment restored INSR signaling as measured by S6 phosphorylation, preserved photoreceptor synaptic connectivity, and more importantly, extended visual function in a murine model of RP.

Methods

Animals

The *rd10* mouse is an autosomal recessive homozygous mutant carrying a human mutation in the phosphodiesterase 6b (*Pde6b*^{*rd10/rd10*}) on a C57BL/6J background [26]. Both *rd10* and wild type (WT) control mice of the same background were obtained from The Jackson Laboratory (Bar Harbor, ME, USA). All animals were housed and handled in accordance with the ARVO statement for the Use of Animals in Ophthalmic and Vision Research, European Union guidelines, and those of the local ethics committees of the CSIC and the Comunidad de Madrid (Spain). Mice were bred in the CIB core facilities on a 12/12-h light/dark cycle. Light intensity was maintained at 3–5 lx.

Generation and administration of adeno-associated viral vectors

Recombinant AAV serotype 2/1 viral vectors bearing cDNA from the human proinsulin (hPi) gene under control of the cytomegalovirus promoter (AAV-hPi) or without hPi cDNA (AAV-null) were generated in the Center for Animal Biotechnology and Gene Therapy at the Universitat Autònoma de Barcelona, as previously described [27]. *rd10* mice received a single intramuscular injection of 7.2×10^{11} vector genomes/kg body weight of AAV-hPi or AAV-null at P10–12. The total vector dose was distributed equally between the gastrocnemius muscles of both hindlimbs.

Measurement of proinsulin, insulin, and glycaemia

Serum, eye, and retinal levels of hPi and serum levels of human insulin were measured using human Pi and human insulin ELISA kits (EZHPi-15K and EZHI-14K, respectively; Millipore, Darmstadt, Germany) according to the manufacturer's instructions and as described previously [25]. Glycaemia was directly measured in blood samples using the Glucocard™ Gmeter kit (A. Menarini Diagnostics Ltd., Berkshire, UK).

RNA isolation and RT-PCR

Total RNA from tissues was isolated using Trizol reagent (Invitrogen). The reverse transcriptase reaction (RT) was typically performed with 2 µg RNA, the Superscript III Kit, and random primers (all from ThermoFisher Scientific, Waltham, MA), followed by amplification with the 2X PANGEA-Long PCR Master Mix (Canvax Biotech, Córdoba, Spain). Mouse *Insr* was amplified using the following primers: sense, 5'-GGCCAGTGAGTGCTGCTCATGC-3' (inside exon 10); antisense, 5'-TGTGGTGGCTGTACATTCC-3' (inside exon 12). Mouse β -actin was amplified using the following primers: sense, 5'-AAGGCCAACCGTGAAAAGAT-3'; antisense, 5'-GTGGTACGACCAGAGGCATAC-3'.

Immunofluorescence and image analysis

Animals were euthanized and their eyes enucleated and fixed for 50 minutes in freshly prepared 4% paraformaldehyde in Sørensen's phosphate buffer (SPB) (0.1 M, pH 7.4), and then cryoprotected by incubation in increasing concentrations of sucrose (final concentration, 50% in SPB). The eyes were then embedded in Tissue-Tek OCT (Sakura Finetec, Torrance, CA, USA) and snap frozen in dry-ice cold isopentane. Equatorial sections (12 µm) were cut on a cryostat and mounted on Superfrost Plus slides (Thermo Scientific, Massachusetts, USA), dried at room temperature, and stored at -20°C until the day of the assay.

Before performing further analyses, slides were dried at room temperature. After rinsing in PBS and permeation with 0.2% (w/v) Triton X-100 in PBS, sections were incubated with blocking buffer (5% normal goat serum, 1% Tween-20, 1 M glycine in PBS) for 1 h and then incubated overnight at 4°C with primary antibodies (Table 1) diluted in blocking buffer. Sections incubated in the absence of primary antibody were used as specificity controls. After rinsing in PBS and incubation with the appropriate secondary antibodies (Supplementary Table 1), sections were stained with DAPI (4',6-diamidino-2-phenylindole; Sigma-Aldrich Corp., St. Louis, MO, USA) and cover slipped with Fluoromont-G. For GluA2 and mGluR6 immunostaining, an antigen retrieval step was performed prior to incubation in blocking buffer. To this end, sections were incubated in citrate buffer (10 mM sodium citrate, 0.05% Tween-20, pH 6.0) in boiling water for 10 minutes. After cooling to room temperature, sections were rinsed with PBS and then incubated in freshly prepared 0.2% sodium borohydride in PBS before continuing with the blocking reaction described above.

Sections were analyzed using a laser confocal microscope (TCS SP5 and TCS SP8; Leica Microsystems, Wetzlar, Germany). In all cases, retinal sections to be compared were stained and imaged under identical conditions. To measure the area occupied by INSR and NF-M immunostaining, images were converted to black and white and analyzed with Fiji software. To quantify the number of horizontal cell tips with associated pS6^{Ser240/244} punctate staining, over 200 horizontal cell tips per animal in 4 retinal areas were analyzed. Similarly, for synapse quantification, over 200 rod ribbons per animal in 4 retinal areas were assessed for associated GluA2 (horizontal cell postsynaptic terminal) or mGluR6 (horizontal cell postsynaptic terminal) punctate immunostaining. To evaluate photoreceptor preservation, three sections per retina were analyzed: for each section, six areas in a nasotemporal sequence were photographed (Fig. 7A). ONL and INL thickness were measured in three random positions for each image.

Transmission electron microscopy

Animals were euthanized and their eyes enucleated and fixed overnight in freshly prepared 2% paraformaldehyde and 2% glutaraldehyde in sodium cacodylate buffer (0.1 M, pH 7.4). After dissection of the cornea and lens, optic cups were post-fixed for 1 hour with 1% OsO₄ (v/v) and 1% K₃Fe(CN)₆ (v/v) in ultrapure water, dehydrated through a graded series of ethanol solutions and embedded in Epoxy EMBED-812 resin (EMS, Electron Microscopy Sciences). Semi-thin (0.5 μm) and ultra-thin sections were obtained using an Ultracut E ultramicrotome (Leica). Semi-thin sections were stained with Toluidine Blue and mounted with Entellan and images were obtained using a light microscope (Axio Observer Z1, Zeiss) with 20× and 100× oil immersion objectives. Ultra-thin sections were contrasted with uranyl acetate and lead citrate, and analyzed at the NUCLEUS electron microscopy facility at the University of Salamanca using a Tecnai Spirit Twin 120 kv electron microscope with a CCD Gatan Orius SC200D camera with DigitalMicrograph™ software. The proportions of the different types of synapses were quantified in ultra-thin sections from 3 mice of each genotype by analyzing over 60 synapses per mouse.

ERG recordings and optomotor tests

Mice were handled and ERGs performed as previously described [23]. Measurements and data analysis were performed by two independent observers, both of them blind to experimental condition. ERG signals were amplified and band filtered between 0.3 and 1000 Hz (CP511 Preamplifier, Grass Instruments, Quincy, MA, USA) and digitized to 10 kHz using a PowerLab acquisition data card (AD Instruments Ltd., Oxfordshire, UK). Graphical representations of the signals recorded and luminous stimuli control were performed with Scope v6.4 PowerLab software (AD Instruments, Oxford, UK). ERG wave amplitudes were measured off-line and the results averaged. Wave amplitude analysis was performed using the MATLAB application.

An optomotor device was built based on the design proposed by Prusky et al. [28]. Measurements and data analysis were performed by two independent observers, both of them blind to experimental condition. Mice were placed in the center of a square array of computer monitors that displayed stimulus gratings, and then monitored using an overhead infrared television camera placed above the testing chamber. The test started with the most easily visible stimulus, with a spatial frequency of 0.088 cycles/degree, a temporal frequency of 0.88 Hz, and a normalized contrast of 1. Contrast sensitivity was calculated as the inverse of contrast threshold, and was measured at distinct spatial frequencies ranging from 0.022–0.355 cycles/degree (Fig. 10B). The Vision Egg tool was used for light stimulation. Stimuli consisted of vertical black/white bars (gratings) moving through the screens.

Statistical analysis

Statistical analysis was performed with GraphPad Prism software 8.0 (GraphPad Software Inc., La Jolla, CA, USA).

To compare two groups, normality was assessed for each group using the Shapiro-Wilk normality test. Normally distributed data were analyzed using an unpaired T-test, and non-normally distributed data using a Mann Whitney U-test. Homocedasticity for all data sets was assessed employing F test. When variance between data sets was significantly different Welch's correction was applied to the T-test. Unpaired T-tests were used to compare insulin receptor and pS6^{Ser240/244} levels between WT and *rd10* animals, and to assess rod-horizontal and rod-bipolar connectivity in AAV-null and AAV-hPi mice.

Analysis of variables over time was achieved using a 1-way ANOVA. Dunnett's multiple comparison test was used to compare values at different time points with those at a specific time point. Accordingly, serum, eye and retinal hPi levels at different time points were compared with initial values using Dunnett's multiple comparison test.

Comparisons of two variables were performed using a 2-way ANOVA, followed by Sidak's multiple comparison test where a significant interaction was detected. Sidak's multiple comparison test was thus used to compare the different synaptic morphologies between WT and *rd10* animals. Differences in histological parameters (ONL/INL ratio), ERG wave amplitude, and optomotor test results between AAV-null mice and AAV-hPi mice were assessed using a 2-way ANOVA.

In all cases, statistical significance was set at $p \leq 0.05$.

Results

Insulin receptor expression and signaling in WT and rd10 retinas

The insulin receptor gene (*Insr*) is expressed in mammals as two differentially spliced mRNA isoforms that differ by the presence of a small exon (exon 11) encoding 12 amino acids at the C-terminal of the α -subunit [29, 30]. The two isoforms (INSR-A and INSR-B) have distinct biochemical and functional properties and tissue distributions [30]. To first characterize the possible role of INSR signaling in the dystrophic retina, we evaluated the retinal expression of each isoform in both physiological and pathological conditions: retinal *Insr-a* and *Insr-b* expression was analyzed by reverse transcriptase polymerase chain reaction (RT-PCR) in WT mice and in the *Pde6b^{rd10/rd10}* (*rd10*) mouse model of RP [26]. Retinal RNA extracts were obtained at different stages from postnatal day 15 (P15) (i.e. before the appearance of evident retinal degeneration) up to P60 (after rod loss) (Fig. 1a). The *Insr-a* isoform, which lacks exon 11, was the only isoform detected in both WT and *rd10* retinas at all stages analyzed, as well as in the three adult WT brain areas analyzed (cerebellum, brainstem, remainder of the telencephalon-diencephalon and olfactory bulb). Conversely, key glucoregulatory tissues, such as the liver and adipose tissue, preferentially expressed the *Insr-b* isoform, which contains exon 11.

INSR tissue distribution was visualized by immunofluorescence using the anti-INSR β -subunit antibody C19 (see Supplementary Table 1). The specificity of this antibody in neural tissue has been previously confirmed in *Insr*-knockout mice [31, 32]. We found that INSR was widely distributed in the WT retina, in accordance with its versatile role in the CNS. Interestingly, we observed prominent expression in the outer plexiform layer (OPL) and the retinal nerve fiber layer (NFL) (Fig. 1b). The OPL is a synaptic layer in which photoreceptor, horizontal, and bipolar cell axons and dendrites connect. Double immunostaining for INSR and calbindin, a marker of horizontal cells, revealed that INSR expression in the OPL was restricted to a subset of calbindin-positive fibers (Fig. 1c). By contrast, we observed no colocalization of INSR and PKC- α , which labels the dendrites of ON-bipolar cells (Additional file 1: Figure S1a). To determine the type (axon or dendrite) of INSR-positive horizontal cell processes, we performed immunostaining for neurofilament M (NF-M), which is selectively expressed by the axons [33, 34] (Fig. 1e). INSR expression in the OPL was restricted to NF-M-positive horizontal cell axons (Fig. 1d). NF-M-positive ganglion cell axons also showed robust INSR expression (Additional file 1: Figure S1b). Horizontal cells receive rod and cone inputs separately; while their axon terminals receive inputs from rods, their dendrites collect input from cone pedicles [34–37]. Therefore, our results indicate preferential expression of INSR in the horizontal cell axons that synapse with rod spherules.

Next, we sought to characterize the pattern of INSR expression associated with retinal dystrophy. In early disease stages, before the onset of any significant disturbances in rod cells (P16), comparable global patterns of INSR immunostaining were observed in WT and *rd10* retinas (Suppl. Figure 2a and b). However, during the course of rod degeneration (P21–P23) we observed a selective and progressive

decrease in INSR immunostaining in horizontal cell axons in the *rd10* retina (Fig. 2). This decrease was not due to the loss of horizontal cells, since similar numbers of calbindin-positive cells were observed in WT and *rd10* retinas at these ages (Additional file 3: Figure S3), nor due to degeneration of horizontal cell axons, as evidenced by the preservation of NF-M immunostaining (Fig. 2). Moreover, INSR downregulation was specific to horizontal cell axons; we observed no significant changes in INSR immunostaining in ganglion cell axons (Fig. 2).

We next investigated whether the selective decrease in INSR expression in horizontal cell axons had consequences at the level of local INSR signaling. Of the multiple downstream effectors of INSR signaling, we specifically focused on ribosomal protein S6. A recent study [38] reported robust pS6^{Ser240/244} immunostaining in retinal horizontal and ganglion cells, where we observed prominent INSR expression. Immunostaining of WT retinas for pS6^{Ser240/244} corroborated the aforementioned labeling of horizontal and ganglion cell bodies (Fig. 3a, upper panels and Additional file 4: Figure S4). Moreover, a closer examination of pS6^{Ser240/244} staining in the OPL revealed profuse punctate labeling in close apposition to the horizontal cell terminal tips (Fig. 3a, upper panels). Interestingly, pS6^{Ser240/244} immunostaining in the *rd10* retina revealed similar staining of horizontal cell bodies, but a dramatic decrease in punctate labeling (Fig. 3a). Double immunostaining for pS6^{Ser240/244} and calbindin showed a decrease in the number of calbindin-positive tips due to retraction of horizontal terminal fibers caused by photoreceptor loss [3, 4]. Moreover, in the *rd10* retina half of the remaining horizontal cell terminal tips were devoid of pS6^{Ser240/244} labeling (Fig. 3a, lower panels and Fig. 3b).

Taken together, our results indicate that in parallel with the degeneration of rod photoreceptors, the terminals of their post-synaptic horizontal cell partners undergo a putative process of insulin resistance, as evidenced by the decreases in INSR levels and pS6^{Ser240/244} signaling. This process may resemble the central and peripheral insulin resistance that occurs in brain neurodegenerative conditions and in type 2 diabetes [6, 39].

Analysis of synaptic ultrastructure in the OPL of WT and rd10 retinas

Given the marked downregulation of INSR expression and signaling in horizontal cell axons and terminal tips that accompanies rod degeneration, together with the role of INSR in synapse formation and maintenance [8, 14, 15], we next investigated whether changes in INSR expression coincided with alterations in synaptic structure in the OPL. Our analyses focused on rod synapses, since cone survival remains uncompromised in the early stages of degeneration in the *rd10* retina [40]. The OPL contains so-called triad synapses, formed by the presynaptic rod spherule, two lateral horizontal, and one or two central bipolar postsynaptic terminals invaginating in close apposition to the synaptic ribbon (Fig. 3a and c). Using electron microscopy, we examined WT and *rd10* retinas in the early stages of degeneration (P21), when a large proportion of rod photoreceptor cells persist but signs of degeneration are also evident (Additional file 5: Figure S5). In WT retinas, most of the rod synapses (70%) corresponded to characteristic triad synapses (Fig. 4a and d). Conversely, in *rd10* retinas at the same timepoint, triad synapses accounted for less than 20% of all synapses (Fig. 4d). Moreover, in *rd10* retinas more than 40%

of rod terminals lacked any postsynaptic element while in WT retinas this was observed in only 8% of rod terminals (Fig. 4b and d). Despite the absence of postsynaptic partners, disconnected rod spherules had a viable appearance, as evidenced by intact mitochondria and electro-lucent content. In these disconnected spherules the synaptic ribbon, when present, was attached to an unusually flat cell membrane with no signs of any postsynaptic invagination (Fig. 4b). By contrast, the degenerative rod spherules (accounting for 20% and 3% of rod terminals in *rd10* and WT retinas, respectively) were highly vacuolated, with electro-dense content and aberrant mitochondria (Fig. 4b and d). Among the degenerated rod spherules we observed both disconnected terminals and triad synapses (Fig. 4b), suggesting that disconnection is not a necessary step before degeneration. Furthermore, both genotypes showed similar numbers of dyads (Additional file 6: Figure S6), most likely due to the misalignment of one of the postsynaptic elements with the plane of section [41].

Immunostaining using specific markers for photoreceptor ribbon (Ribeye and Ctbp2) and horizontal (GluA2) and bipolar (mGluR6) postsynaptic terminal tips also revealed synaptic disconnection of rod photoreceptors (Additional file 7: Figure S7).

Systemic proinsulin reaches the retina and exerts no metabolic effect

The results described above suggest a possible link between deficient INSR signaling, synaptic disconnection in rod photoreceptors, and the visual impairment characteristic of RP. To determine whether deficient INSR signaling is a disease-modifying factor in RP, and therefore a potential therapeutic target, we employed a gene therapy strategy to enhance INSR signaling. Proinsulin, the insulin precursor, is an INSR-A selective ligand [42] with a low metabolic profile, likely due to its poor affinity for the INSR-B isoform [30, 42]. We have previously demonstrated the neuroprotective potential of Pi during retinal development and degeneration [23–25, 43]. Given that treatment of RP in humans would entail long-term administration, we selected Pi to activate INSR-A, the predominant INSR isoform expressed in the retina (Fig. 1a).

To achieve sustained production of Pi, we built upon our previous experience with a recombinant AAV2/1 expressing the human proinsulin (hPi) coding region (Fig. 5; AAV-hPi) [24, 27]. We first evaluated hPi production following intramuscular administration of AAV-hPi. *rd10* mice received a single injection of AAV-hPi into the gastrocnemius muscle at P10 to induce hPi production before the onset of degeneration (around P18). In AAV-hPi-treated *rd10* mice hPi serum levels were uniformly sustained within each individual mouse for up to 5 months (the maximum follow-up period) (Fig. 5b). Moreover, hPi was detected in whole eye and in retinal extracts as early as 1 week post-injection and up to 7 weeks post-injection (the maximum follow-up period) (Additional file 8: Figure S8a). Conversely, hPi was not detected at any timepoint in serum samples, whole eye, or retinal extracts from mice injected with the control vector (AAV-null). Moreover, mature human insulin was absent in serum samples from AAV-hPi-treated WT mice, in agreement with our previous findings [24, 27]. Therefore, Pi produced from AAV-hPi remained mainly, if not completely, unprocessed. Importantly, we observed no differences in glycaemia or body weight in AAV-hPi- versus AAV-null-treated mice (Fig. 5c and d), confirming an absence of significant

metabolic effects of systemic hPi production, in line with previous studies (Corrochano et al., 2008; Fernández-Sánchez et al., 2012; Corpas et al. 2017).

AAV-hPi treatment in rd10 mice preserves photoreceptors and photoreceptor synaptic connectivity

To determine the effect of hPi on the dystrophic retina, we first examined whether hPi treatment could restore INSR signaling. AAV-hPi treated *rd10* retinas exhibited higher levels of punctate pS6^{Ser240/244} staining in the OPL than control (AAV-null-treated) *rd10* retinas (Fig. 6). Quantification of the number of pS6^{Ser240/244}-positive horizontal cell tips at P21 showed that hPi treatment increased the proportion of calbindin-pS6^{Ser240/244}-positive tips to near 90%, close to the proportion observed in WT retinas (Fig. 3). By contrast, in control (AAV-null-treated) *rd10* retinas the proportion of pS6^{Ser240/244}-positive horizontal cell tips remained in the range of 50–60% (Fig. 6b). In addition, we observed a greater abundance of total calbindin-positive tips in the AAV-hPi-treated than in the control retinas, most likely a consequence of photoreceptor preservation caused by hPi treatment (Fig. 7).

We next investigated whether long-term hPi treatment exerted a neuroprotective effect. To this end, we injected *rd10* mice with AAV-null or AAV-hPi at P10–P12 and analyzed the corresponding retinas at P30, at which point most photoreceptor cells have been lost in this mouse model. Two distinct histological parameters were evaluated: photoreceptor cell preservation and synapse maintenance. AAV-hPi-treated *rd10* retinas showed modest but significant photoreceptor preservation, as determined by measuring the relative increase in thickness of the outer nuclear layer (ONL), an effect that was more evident in the nasal peripheral retina (T1; Fig. 7). In parallel, the synaptic connectivity of photoreceptors was assessed by immunostaining rod-bipolar and rod-horizontal synapses. As expected, photoreceptor preservation in AAV-hPi-treated retinas led to an increase in the number of ribbons. Moreover, hPi reduced the proportion of disconnected postsynaptic terminals of rod cells (i.e. those lacking either a GluA2-positive horizontal postsynaptic terminal [Fig. 8a and c] or a mGluR6-positive bipolar postsynaptic terminal [Fig. 8b and d]). These results reveal a novel effect of proinsulin: preservation of the synaptic connectivity of rod cells with their postsynaptic second-order neuronal partners. This observation suggests a second distinct role of hPi that may be partially independent of its effects on photoreceptor cell survival revealed in our previous studies [23–25]. Moreover, the increase in the number of photoreceptor synapses induced by proinsulin treatment that we previously observed in the P23H rat model of RP [24] is most likely a consequence of the rescue of photoreceptor cells as well as preservation of their synaptic contacts, as described here.

AAV-hPi treatment in rd10 mice preserves visual function

Finally, in AAV-hPi-treated *rd10* mice we assessed whether hPi preserved visual function, which is the most clinically relevant outcome for a potential RP treatment. Electroretinographic (ERG) recordings were performed in dim and daylight conditions every 10 days between P30 and P60 to evaluate rod- and cone-mediated light responses (Fig. 9). AAV-hPi-treated *rd10* mice displayed better defined and more prominent ERG waves than their AAV-null-treated counterparts (Fig. 9b). Waves corresponding to rods (b-scotopic wave), cones (b-photopic wave), and both photoreceptors (a-mixed and b-mixed waves) were of a

significantly greater amplitude in AAV-hPi-treated than AAV-null-treated *rd10* mice (Fig. 9c). ERG recordings thus confirmed that hPi treatment preserved visual function, consistent with the aforementioned preservation of photoreceptor cells and their synapses. Optokinetic testing further confirmed partial preservation of the light response in AAV-hPi-treated *rd10* retinas. In addition to measuring the retinal response to light, this visual behavior test evaluates the function of other components of the visual system, namely optic nerve transmission and visual integration in the brain [44]. Mice instinctively respond to rotating vertical bars with characteristic movement of their heads in the same direction as the rotation of the bar (Fig. 10a and b). AAV-hPi-treated *rd10* mice showed greater contrast sensitivity than AAV-null-treated counterparts at the two ages studied (P40 and P50; Fig. 10c and d). Together, our results support the disease-modifying potential of Pi, which can prolong visual function in an animal model of RP and therefore constitutes a viable candidate therapy for retinal dystrophies.

Discussion

This study describes the downregulation of retinal INSR levels and local signaling during the early stages of retinal neurodegeneration in the *rd10* mouse model of RP, together with concomitant disruption of photoreceptor triad synapses. These findings suggest that deterioration of INSR signaling contributes to the structural and functional degeneration of the retina in *rd10* mice. We provide proof of concept of the neuroprotective effect of INSR stimulation with the insulin precursor Pi, which is selective for the INSR-A isoform found in the retina. Gene therapy using an AAV induced sustained production of circulating Pi, which reached the retina, restored local INSR signaling, and exerted neuroprotective effects on retinal structure and visual function, without affecting peripheral metabolic parameters. Proinsulin treatment attenuated both photoreceptor cell loss and synaptic disconnection, and prolonged visual function, highlighting the potential of Pi as a candidate therapy for RP.

Studies over the past two decades have broadened the scope of INSR activity far beyond the peripheral metabolic role initially ascribed to this receptor. The versatility of this receptor is also implied by its widespread expression in the CNS. At the neuronal level, INSR has been implicated in synaptic plasticity, dendritic outgrowth, and cell survival [8, 14, 15]. The *Insr-a* splice variant, which is predominantly expressed in different areas of the brain as well as the retina, is the most ancient and promiscuous isoform, and participates in insulin, Pi, and IGF-II signaling [29, 42]. Interestingly, many of the signaling pathways in which INSR-A is involved are similar to those mediated by growth factor receptors, and in some ways this isoform resembles the ancestral INSR expressed in invertebrates and low vertebrates [7, 45, 46]. The present findings confirm the previously described wide distribution of INSR in the WT retina [47, 48]. However, we also describe for the first time more intense INSR immunostaining in horizontal and ganglion cell axons than in other retinal structures. Interestingly, analysis of INSR expression during retinal degeneration in the *rd10* mouse revealed local downregulation of INSR, specifically in horizontal cell axons. This was accompanied by a decrease in the phosphorylation of ribosomal protein S6 in horizontal cell terminals, indicating impaired INSR signaling. Notably, horizontal cell axon terminals receive input from the rod photoreceptors, the main targets of degeneration in RP. A recent study by

Agostinone et al. [38] reported specific decreases in pS6^{Ser240/244} in ganglion cells following transection of their axons, but no alterations in pS6^{Ser240/244} in horizontal cells. In the present study, we observed selective downregulation of INSR expression and impaired signaling in the horizontal cells with which the damaged rod photoreceptors synapse. It remains unclear whether this finding is mechanistically linked to the decreases in pS6^{Ser240/244} described by Agostinone et al [38]. However, our results are consistent with the proposals by other authors that INSR signaling may vary in a neuronal activity-dependent manner [8, 49, 50], and suggest that INSR expression and signaling in horizontal cells may depend on rod input.

Interestingly, in *rd10* retinas INSR downregulation and consequent impairment of INSR signaling coincided with the presence of disconnected but otherwise apparently viable rod terminals. Alterations in retinal synaptic circuitry as part of retinal remodeling during photoreceptor degeneration have been acknowledged for more than two decades [3, 51–53]. De-afferentiation of second-order neurons has typically been described in advanced stages of degeneration as a consequence of photoreceptor loss [3, 51–53]. However, here we describe early disconnection events affecting up to 50% of apparently viable rod spherules during the initial stages of degeneration. Although further studies will be required to clarify the consequences of this disconnection, it does not appear to necessarily precede rod death, as we detected degenerative triads containing the presynaptic rod spherule and horizontal and bipolar terminals. These observations have direct implications for the development of neuroprotective therapies and could open a new line of research into interventions aimed at preserving rod connectivity.

Our findings demonstrate the potential of Pi as a synaptoprotective factor. In *rd10* mice treated with AAV-hPi, systemically produced Pi reached the retina and restored INSR signaling, as determined by measuring pS6^{Ser240/244} levels. Concomitantly, Pi treatment reduced the number of disconnected rod presynaptic terminals, supporting a role of INSR signaling in photoreceptor synaptic connectivity. Our results are in line with those of the seminal study by Chiu et al. 2008 [8], who used optic tectal neurons in living *Xenopus* tadpoles to demonstrate that INSR signaling maintains both synaptic contacts and the branches on which they lie. Moreover, in the aforementioned study by Agostinone et al. [38] stimulation of INSR signaling with insulin promoted regeneration of the dendritic arbors of retinal ganglion cells after axonal injury.

Deficient local INSR signaling associated with RP may be a general feature of neurodegenerative diseases, irrespective of peripheral insulin resistance [reviewed in [6]]. Several studies have described decreased INSR expression and/or attenuation of the activation states of INSR signaling molecules in affected brain regions in patients with Alzheimer's [17–19] and Parkinson's [54–56] diseases. We show that pharmacological stimulation of INSR signaling with Pi has a disease-modifying effect over the course of retinal degeneration, in line with the beneficial effects of INSR stimulation with insulin reported in other neurodegenerative diseases of the brain and retina [6, 38, 39]. Moreover, the widespread expression of INSR in the retina suggests that synaptic maintenance promoted by INSR signaling is only one of several retinal processes regulated by INSR. Indeed, we and others have demonstrated the neuroprotective effects of INSR signaling molecules on photoreceptor survival [57–59].

Conclusion

Our results provide a novel mechanism to account for our previous descriptions of the neuroprotective effects of Pi on retinal dystrophy [23–25] and cognitive impairment [27], and further support the validity of Pi-mediated stimulation of INSR as a candidate therapy for neurodegenerative conditions of the CNS.

Abbreviations

AAV: Adeno-associated viral vector; ANOVA: Analysis of variance; CNS: Central nervous system; Ctbp2: c-terminal binding protein 2; ELISA: Enzyme-Linked ImmunoSorbent Assay; ERG: Electroretinographic recording; GCL: Ganglion cell layer; GluA2: ionotropic glutamate receptor A2; hPi: human proinsulin; INL: Inner nuclear layer; INSR/*Insr*: Insulin receptor; IPL: Inner plexiform layer; mGluR6: metabotropic glutamate receptor 6; NFL: Nerve fiber layer; NF-M: Neurofilament medium; ONL: Outer nuclear layer; OPL: Outer plexiform layer; P: post-natal day; PBS: Phosphate buffer saline; PKC- α : protein kinase C alpha; RP: Retinitis pigmentosa; RT-PCR: reverse transcriptase polymerase chain reaction; S6: ribosomal S6 protein; SPB: Sørensen's phosphate buffer; WT: Wild type.

Declarations

Availability of data and materials

The datasets used and/or analyzed during the current study are available from the corresponding author on reasonable request.

Competing interest

Authors do not have competing interests.

Consent for publication

All authors consent for the publication of this study.

Ethical approval and consent to participate

Animal handling and experimental procedures followed the 3Rs principles, and were revised by the Animal Welfare Committee of the Centro de Investigaciones Biológicas (CIB) and the Bioethics Committee of the Consejo Superior de Investigaciones Científicas (CSIC) and authorized by the Comunidad de Madrid (Ref: PROEX 157/14), in accordance with the Spanish legislation and the European Union (EU) Directive 2010/63/EU for animal research.

Funding

This work was supported by grants from the Spanish MINECO (SAF2013-41059-R and SAF2016-75681-R to EJdIR, PI13-02098 to PdIV), the Instituto de Salud Carlos III and co-financed by the European Development Regional Fund “A way to make Europe”/“Investing in your future” (ERDF/ESF) (PI17/01601 to IL and PI18/01536 to CL), the Instituto de Salud Carlos III RETICS RD16/0019/0009 and the Madrid Regional Government B2017/BMD-3688 to IL.

Author's contributions

ASC, AHP, CI and MM performed experimental procedures. CL carried out and analyzed the electron microscopy studies. PdIV designed the functional studies and analyzed the data. FB designed and generated the AAV vectors. EJdIR and CHS designed and supervised the biological experiments. EJdIR and CHS analyzed and discussed the results. ASC, CL, CI, IL, PdIV, FB, EJdIR and CHS contributed to the writing and editing of the manuscript. All authors read and approved the final manuscript.

Acknowledgements

The authors thank Cayetana Murillo, María D. Hernández-Fuentes, the staff at the CIB animal facility and CIB and UCM microscopy facilities for technical support; Nuria Forns and Ryan Steel for setting the conditions for the optomotor test and for synapse immunostaining; Noemi Alvarez Lindo for designing the diagrams; and José A. Esteban for supplying the anti-Glu2A antibody. ASC is recipient of a UCM predoctoral fellowship (CT45/15).

Notes

Enrique J de la Rosa and Catalina Hernández-Sánchez contributed equally to the publication.

References

1. Collaborators GBDN. Global, regional, and national burden of neurological disorders, 1990–2016: a systematic analysis for the Global Burden of Disease Study 2016. *Lancet Neurol.* 2019;18:459–80.
2. de La Rosa EJ, Hernandez-Sanchez C: *CNS Targets for the Treatment of Retinal Dystrophies: A Win-Win Strategy. Therapies for retinal degeneration: targeting common processes.* Royal Society of Chemistry; 2018.
3. Pfeiffer RL, Marc RE, Jones BW. Persistent remodeling and neurodegeneration in late-stage retinal degeneration. *Prog Retin Eye Res.* 2020;74:100771.
4. Cuenca N, Fernandez-Sanchez L, Campello L, Maneu V, De la Villa P, Lax P, Pinilla I. Cellular responses following retinal injuries and therapeutic approaches for neurodegenerative diseases. *Prog Retin Eye Res.* 2014;43:17–75.

5. Russell S, Bennett J, Wellman JA, Chung DC, Yu ZF, Tillman A, Wittes J, Pappas J, Elci O, McCague S, et al. Efficacy and safety of voretigene neparvovec (AAV2-hRPE65v2) in patients with RPE65-mediated inherited retinal dystrophy: a randomised, controlled, open-label, phase 3 trial. *Lancet*. 2017;390:849–60.
6. Arnold SE, Arvanitakis Z, Macauley-Rambach SL, Koenig AM, Wang HY, Ahima RS, Craft S, Gandy S, Buettner C, Stoeckel LE, et al. Brain insulin resistance in type 2 diabetes and Alzheimer disease: concepts and conundrums. *Nat Rev Neurol*. 2018;14:168–81.
7. Banks WA, Owen JB, Erickson MA. Insulin in the brain: there and back again. *Pharmacol Ther*. 2012;136:82–93.
8. Chiu SL, Cline HT. Insulin receptor signaling in the development of neuronal structure and function. *Neural Dev*. 2010;5:7.
9. de la Rosa EJ, Bondy CA, Hernandez-Sanchez C, Wu X, Zhou J, Lopez-Carranza A, Scavo LM, de Pablo F. Insulin and insulin-like growth factor system components gene expression in the chicken retina from early neurogenesis until late development and their effect on neuroepithelial cells. *Eur J Neurosci*. 1994;6:1801–10.
10. Havrankova J, Roth J, Brownstein M. Insulin receptors are widely distributed in the central nervous system of the rat. *Nature*. 1978;272:827–9.
11. Marks JL, Porte D Jr, Stahl WL, Baskin DG. Localization of insulin receptor mRNA in rat brain by in situ hybridization. *Endocrinology*. 1990;127:3234–6.
12. Rodrigues M, Waldbillig RJ, Rajagopalan S, Hackett J, LeRoith D, Chader GJ. Retinal insulin receptors: localization using a polyclonal anti-insulin receptor antibody. *Brain Res*. 1988;443:389–94.
13. Unger J, McNeill TH, Moxley RT 3rd, White M, Moss A, Livingston JN. Distribution of insulin receptor-like immunoreactivity in the rat forebrain. *Neuroscience*. 1989;31:143–57.
14. Gralle M. The neuronal insulin receptor in its environment. *J Neurochem*. 2017;140:359–67.
15. Lee CC, Huang CC, Hsu KS. Insulin promotes dendritic spine and synapse formation by the PI3K/Akt/mTOR and Rac1 signaling pathways. *Neuropharmacology*. 2011;61:867–79.
16. Moloney AM, Griffin RJ, Timmons S, O'Connor R, Ravid R, O'Neill C. Defects in IGF-1 receptor, insulin receptor and IRS-1/2 in Alzheimer's disease indicate possible resistance to IGF-1 and insulin signalling. *Neurobiol Aging*. 2010;31:224–43.
17. Rivera EJ, Goldin A, Fulmer N, Tavares R, Wands JR, de la Monte SM. Insulin and insulin-like growth factor expression and function deteriorate with progression of Alzheimer's disease: link to brain reductions in acetylcholine. *J Alzheimers Dis*. 2005;8:247–68.
18. Steen E, Terry BM, Rivera EJ, Cannon JL, Neely TR, Tavares R, Xu XJ, Wands JR, de la Monte SM. Impaired insulin and insulin-like growth factor expression and signaling mechanisms in Alzheimer's disease—is this type 3 diabetes? *J Alzheimers Dis*. 2005;7:63–80.
19. Talbot K, Wang HY, Kazi H, Han LY, Bakshi KP, Stucky A, Fuino RL, Kawaguchi KR, Samoyedny AJ, Wilson RS, et al. Demonstrated brain insulin resistance in Alzheimer's disease patients is associated with IGF-1 resistance, IRS-1 dysregulation, and cognitive decline. *J Clin Invest*. 2012;122:1316–38.

20. Chapman CD, Schioth HB, Grillo CA, Benedict C. Intranasal insulin in Alzheimer's disease: Food for thought. *Neuropharmacology*. 2018;136:196–201.
21. Hernandez-Sanchez C, Lopez-Carranza A, Alarcon C, de La Rosa EJ, de Pablo F. Autocrine/paracrine role of insulin-related growth factors in neurogenesis: local expression and effects on cell proliferation and differentiation in retina. *Proc Natl Acad Sci U S A*. 1995;92:9834–8.
22. Valenciano AI, Corrochano S, de Pablo F, de la Villa P, de la Rosa EJ. Proinsulin/insulin is synthesized locally and prevents caspase- and cathepsin-mediated cell death in the embryonic mouse retina. *J Neurochem*. 2006;99:524–36.
23. Corrochano S, Barhoum R, Boya P, Arroba AI, Rodriguez-Muela N, Gomez-Vicente V, Bosch F, de Pablo F, de la Villa P, de la Rosa EJ. Attenuation of vision loss and delay in apoptosis of photoreceptors induced by proinsulin in a mouse model of retinitis pigmentosa. *Invest Ophthalmol Vis Sci*. 2008;49:4188–94.
24. Fernandez-Sanchez L, Lax P, Isiegas C, Ayuso E, Ruiz JM, de la Villa P, Bosch F, de la Rosa EJ, Cuenca N. Proinsulin slows retinal degeneration and vision loss in the P23H rat model of retinitis pigmentosa. *Hum Gene Ther*. 2012;23:1290–300.
25. Isiegas C, Marinich-Madzarevich JA, Marchena M, Ruiz JM, Cano MJ, de la Villa P, Hernandez-Sanchez C, de la Rosa EJ, de Pablo F. Intravitreal Injection of Proinsulin-Loaded Microspheres Delays Photoreceptor Cell Death and Vision Loss in the rd10 Mouse Model of Retinitis Pigmentosa. *Invest Ophthalmol Vis Sci*. 2016;57:3610–8.
26. Chang B, Hawes NL, Pardue MT, German AM, Hurd RE, Davisson MT, Nusinowitz S, Rengarajan K, Boyd AP, Sidney SS, et al. Two mouse retinal degenerations caused by missense mutations in the beta-subunit of rod cGMP phosphodiesterase gene. *Vision Res*. 2007;47:624–33.
27. Corpas R, Hernandez-Pinto AM, Porquet D, Hernandez-Sanchez C, Bosch F, Ortega-Aznar A, Comellas F, de la Rosa EJ, Sanfeliu C. Proinsulin protects against age-related cognitive loss through anti-inflammatory convergent pathways. *Neuropharmacology*. 2017;123:221–32.
28. Prusky GT, Alam NM, Beekman S, Douglas RM. Rapid quantification of adult and developing mouse spatial vision using a virtual optomotor system. *Invest Ophthalmol Vis Sci*. 2004;45:4611–6.
29. Hernandez-Sanchez C, Mansilla A, de Pablo F, Zardoya R. Evolution of the insulin receptor family and receptor isoform expression in vertebrates. *Mol Biol Evol*. 2008;25:1043–53.
30. Belfiore A, Malaguarnera R, Vella V, Lawrence MC, Sciacca L, Frasca F, Morrione A, Vigneri R. Insulin Receptor Isoforms in Physiology and Disease: An Updated View. *Endocr Rev*. 2017;38:379–431.
31. Bruning JC, Gautam D, Burks DJ, Gillette J, Schubert M, Orban PC, Klein R, Krone W, Muller-Wieland D, Kahn CR. Role of brain insulin receptor in control of body weight and reproduction. *Science*. 2000;289:2122–5.
32. Dixon-Salazar TJ, Fourgeaud L, Tyler CM, Poole JR, Park JJ, Boulanger LM. MHC class I limits hippocampal synapse density by inhibiting neuronal insulin receptor signaling. *J Neurosci*. 2014;34:11844–56.

33. Peichl L, Gonzalez-Soriano J. Unexpected presence of neurofilaments in axon-bearing horizontal cells of the mammalian retina. *J Neurosci.* 1993;13:4091–100.
34. Peichl L, Gonzalez-Soriano J. Morphological types of horizontal cell in rodent retinae: a comparison of rat, mouse, gerbil, and guinea pig. *Vis Neurosci.* 1994;11:501–17.
35. Feigenspan A, Babai N. Functional properties of spontaneous excitatory currents and encoding of light/dark transitions in horizontal cells of the mouse retina. *Eur J Neurosci.* 2015;42:2615–32.
36. Kolb H. Organization of the outer plexiform layer of the primate retina: electron microscopy of Golgi-impregnated cells. *Philos Trans R Soc Lond B Biol Sci.* 1970;258:261–83.
37. Kolb H. The connections between horizontal cells and photoreceptors in the retina of the cat: electron microscopy of Golgi preparations. *J Comp Neurol.* 1974;155:1–14.
38. Agostinone J, Alarcon-Martinez L, Gamlin C, Yu WQ, Wong ROL, Di Polo A. Insulin signalling promotes dendrite and synapse regeneration and restores circuit function after axonal injury. *Brain.* 2018;141:1963–80.
39. Holscher C. Brain insulin resistance: role in neurodegenerative disease and potential for targeting. *Expert Opin Investig Drugs.* 2020;29:333–48.
40. Zhao L, Zabel MK, Wang X, Ma W, Shah P, Fariss RN, Qian H, Parkhurst CN, Gan WB, Wong WT. Microglial phagocytosis of living photoreceptors contributes to inherited retinal degeneration. *EMBO Mol Med.* 2015;7:1179–97.
41. Wang T, Pahlberg J, Cafaro J, Frederiksen R, Cooper AJ, Sampath AP, Field GD, Chen J. Activation of Rod Input in a Model of Retinal Degeneration Reverses Retinal Remodeling and Induces Formation of Functional Synapses and Recovery of Visual Signaling in the Adult Retina. *J Neurosci.* 2019;39:6798–810.
42. Malaguarnera R, Sacco A, Voci C, Pandini G, Vigneri R, Belfiore A. Proinsulin binds with high affinity the insulin receptor isoform A and predominantly activates the mitogenic pathway. *Endocrinology.* 2012;153:2152–63.
43. Hernandez-Sanchez C, Mansilla A, de la Rosa EJ, de Pablo F. Proinsulin in development: New roles for an ancient prohormone. *Diabetologia.* 2006;49:1142–50.
44. Abdeljalil J, Hamid M, Abdel-Mouttalib O, Stephane R, Raymond R, Johan A, Jose S, Pierre C, Serge P. The optomotor response: a robust first-line visual screening method for mice. *Vision Res.* 2005;45:1439–46.
45. Belfiore A, Frasca F, Pandini G, Sciacca L, Vigneri R. Insulin receptor isoforms and insulin receptor/insulin-like growth factor receptor hybrids in physiology and disease. *Endocr Rev.* 2009;30:586–623.
46. Chan SJ, Steiner DF: **Insulin Through the Ages: Phylogeny of a Growth Promoting and Metabolic Regulatory Hormone 1.** *American Zoologist, Volume 40, Issue 2, April 2000, Pages 213–222* 2000, **40**:213–222.
47. Gosbell AD, Favilla I, Baxter KM, Jablonski P. Insulin receptor and insulin receptor substrate-I in rat retinae. *Clin Exp Ophthalmol.* 2000;28:212–5.

48. Rajala RV, Wiskur B, Tanito M, Callegan M, Rajala A. Diabetes reduces autophosphorylation of retinal insulin receptor and increases protein-tyrosine phosphatase-1B activity. *Invest Ophthalmol Vis Sci.* 2009;50:1033–40.
49. Clarke DW, Mudd L, Boyd FT Jr, Fields M, Raizada MK. Insulin is released from rat brain neuronal cells in culture. *J Neurochem.* 1986;47:831–6.
50. Hori K, Yasuda H, Konno D, Maruoka H, Tsumoto T, Sobue K. NMDA receptor-dependent synaptic translocation of insulin receptor substrate p53 via protein kinase C signaling. *J Neurosci.* 2005;25:2670–81.
51. Jones BW, Kondo M, Terasaki H, Lin Y, McCall M, Marc RE. Retinal remodeling. *Jpn J Ophthalmol.* 2012;56:289–306.
52. Lewis GP, Linberg KA, Fisher SK. Neurite outgrowth from bipolar and horizontal cells after experimental retinal detachment. *Invest Ophthalmol Vis Sci.* 1998;39:424–34.
53. Strettoi E, Pignatelli V, Rossi C, Porciatti V, Falsini B. Remodeling of second-order neurons in the retina of rd/rd mutant mice. *Vision Res.* 2003;43:867–77.
54. Moroo I, Yamada T, Makino H, Tooyama I, McGeer PL, McGeer EG, Hirayama K. Loss of insulin receptor immunoreactivity from the substantia nigra pars compacta neurons in Parkinson's disease. *Acta Neuropathol.* 1994;87:343–8.
55. Takahashi M, Yamada T, Tooyama I, Moroo I, Kimura H, Yamamoto T, Okada H. Insulin receptor mRNA in the substantia nigra in Parkinson's disease. *Neurosci Lett.* 1996;204:201–4.
56. Timmons S, Coakley MF, Moloney AM, C ON. Akt signal transduction dysfunction in Parkinson's disease. *Neurosci Lett.* 2009;467:30–5.
57. Punzo C, Kornacker K, Cepko CL. Stimulation of the insulin/mTOR pathway delays cone death in a mouse model of retinitis pigmentosa. *Nat Neurosci.* 2009;12:44–52.
58. Rajala A, Tanito M, Le YZ, Kahn CR, Rajala RV. Loss of neuroprotective survival signal in mice lacking insulin receptor gene in rod photoreceptor cells. *J Biol Chem.* 2008;283:19781–92.
59. Sanchez-Cruz A, Villarejo-Zori B, Marchena M, Zaldivar-Diez J, Palomo V, Gil C, Lizasoain I, de la Villa P, Martinez A, de la Rosa EJ, Hernandez-Sanchez C. Modulation of GSK-3 provides cellular and functional neuroprotection in the rd10 mouse model of retinitis pigmentosa. *Mol Neurodegener.* 2018;13:19.

Supplementary Figure Legends

Additional file 1: Figure S1. Analysis of insulin receptor expression. Representative retinal sections collected from WT mice at P21. **a, b.** Magnified image showing the OPL (a) and NFL (b) after co-immunostaining for the indicated markers. Nuclei are stained with DAPI (blue). OPL, outer plexiform layer; NFL, nerve fiber layer. Scale bar: 21 μm .

Additional file 1: Figure S2. Analysis of insulin receptor expression in WT and *rd10* retinas at P16. a. Representative images of P16 retinal sections from WT and *rd10* mice co-immunostained for INSR

(green) and neurofilament-M (NF-M, red). Nuclei are stained with DAPI (blue). ONL, outer nuclear layer; OPL, outer plexiform layer; INL, inner nuclear layer; IPL, inner plexiform layer; NFL, nerve fiber layer. Scale bar: 58 μ m. **b.** Quantification of the area of INSR-positive immunostaining at P16 in retinal sections from WT and *rd10* mice. The area of INSR-positive immunostaining was normalized to that of neurofilament-staining of the same region to correct for potential variation among retinal sections, and to *INSR* immunostaining in WT sections (=1.0). Data are presented as the mean + SEM. n=3 mice, 4 images per retina.

Additional file 1: Figure S3. Comparison of the number of horizontal cells in WT and *rd10* retinas. a. Representative images of P23 retinal sections from WT and *rd10* mice, immunostained for calbindin to label horizontal cells (red). Nuclei are stained with DAPI (blue). **b.** The number of calbindin⁺ cells was scored in equatorial sections in the central regions of the retina (T3–T4; see Methods and Figure 7a). Plots show the mean + SEM. n=5 mice, 10 images per retina. ONL, outer nuclear layer; OPL, outer plexiform layer; INL, inner nuclear layer. Scale bar: 38 μ m.

Additional file 1: Figure S4. Analysis of pS6^{Ser240/244} expression in ganglion cells in WT and *rd10* retinas. Representative images of the GCL of P23 retinal sections from WT and *rd10* mice immunostained for pS6^{Ser240/244} (green). Nuclei are stained with DAPI (blue). Brackets delimit the GCL. GCL, ganglion cell layer. Scale bar: 41 μ m.

Additional file 1: Figure S5. Representative semi-thin retinal sections. a. Semi-thin retinal sections collected at P21 from WT and *rd10* mice were prepared for electron microscopy analysis (Fig. 4d). Scale bar: 50 μ m. **b.** Magnification of the indicated region. Arrows indicate photoreceptor presynaptic terminals. Asterisks indicate degenerating photoreceptors, as evidenced by the condensed nucleus. ONL, outer nuclear layer; OPL, outer plexiform layer; IPL, inner plexiform layer; INL, inner nuclear layer; NFL, nerve fiber layer. Scale bar: 100 μ m.

Additional file 1: Figure S6. Quantification of the proportion of dyads. Data are presented as the mean + SEM. n=3 mice, ≥ 60 synapses per mouse.

Additional file 1: Figure S7. Representative 3D reconstructions of P23 WT and *rd10* synapses in the OPL. a, b. Retinal sections were co-immunostained for Ribeye (ribbon at presynaptic terminal, red) and the glutamate receptor subunit GluA2 (horizontal postsynaptic terminal, green) (a), or for Ctbp2 (ribbon at presynaptic terminal, red) and the glutamate receptor mGluR6 (bipolar postsynaptic terminal, green) (b). Arrowheads indicate ribbons (rod presynaptic terminals) without a post-synaptic partner. Scale bar: 6 μ m.

Additional file 1: Figure S8. Determination of hPi levels after AAV-hPi treatment. *rd10* mice received a single intramuscular injection of AAV-hPi or AAV-null at P10. **a, b.** ELISA was performed to measure hPi in retinal and eye extracts (a) and in serum (b) at the indicated times. Data are presented as the mean + SEM. n=3 mice. * $p \leq 0.05$ (1-way ANOVA with Dunnett's multiple comparison test).

Figures

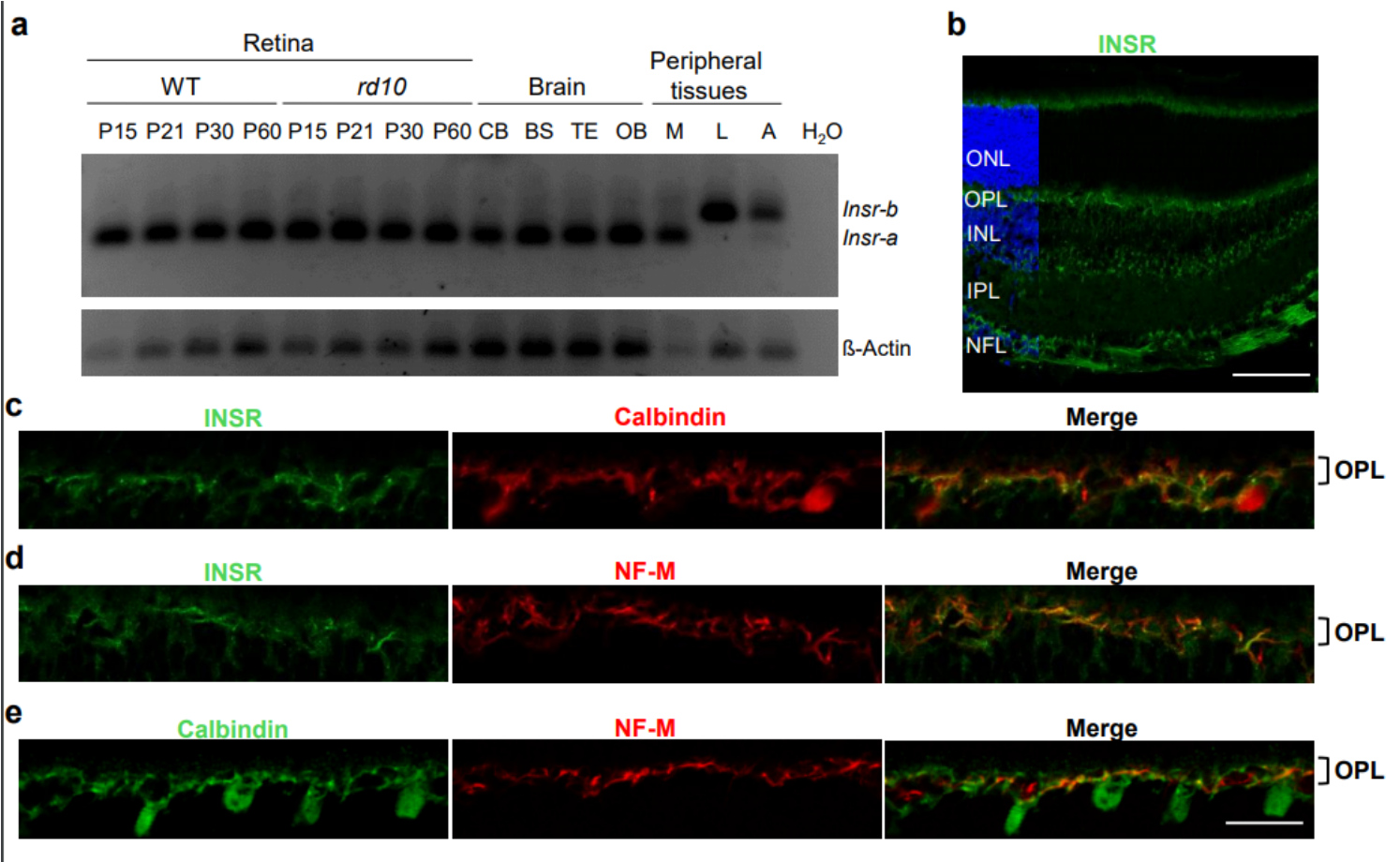


Figure 1

Insulin receptor expression in the retina. a. RT-PCR of WT and *rd10* mouse retinas at the indicated ages, and WT adult brain regions and peripheral tissues. Forward and reverse PCR primers corresponded to exons 10 and 12, respectively, of *Insr*. CB, cerebellum; BS, brain stem; TE, remainder of telencephalon and diencephalon; OB, olfactory bulb; M, muscle; L, liver; A, adipose tissue. β -actin was used as a loading control. b-e. Representative images of P21 retinal sections from WT mice. b, Image of a retinal section immunostained for INSR (green). Nuclei are stained with DAPI (blue). c-e, Magnified image of the OPL showing double immunostaining for the indicated markers. ONL, outer nuclear layer; OPL, outer plexiform layer; INL, inner nuclear layer; IPL, inner plexiform layer; NFL,

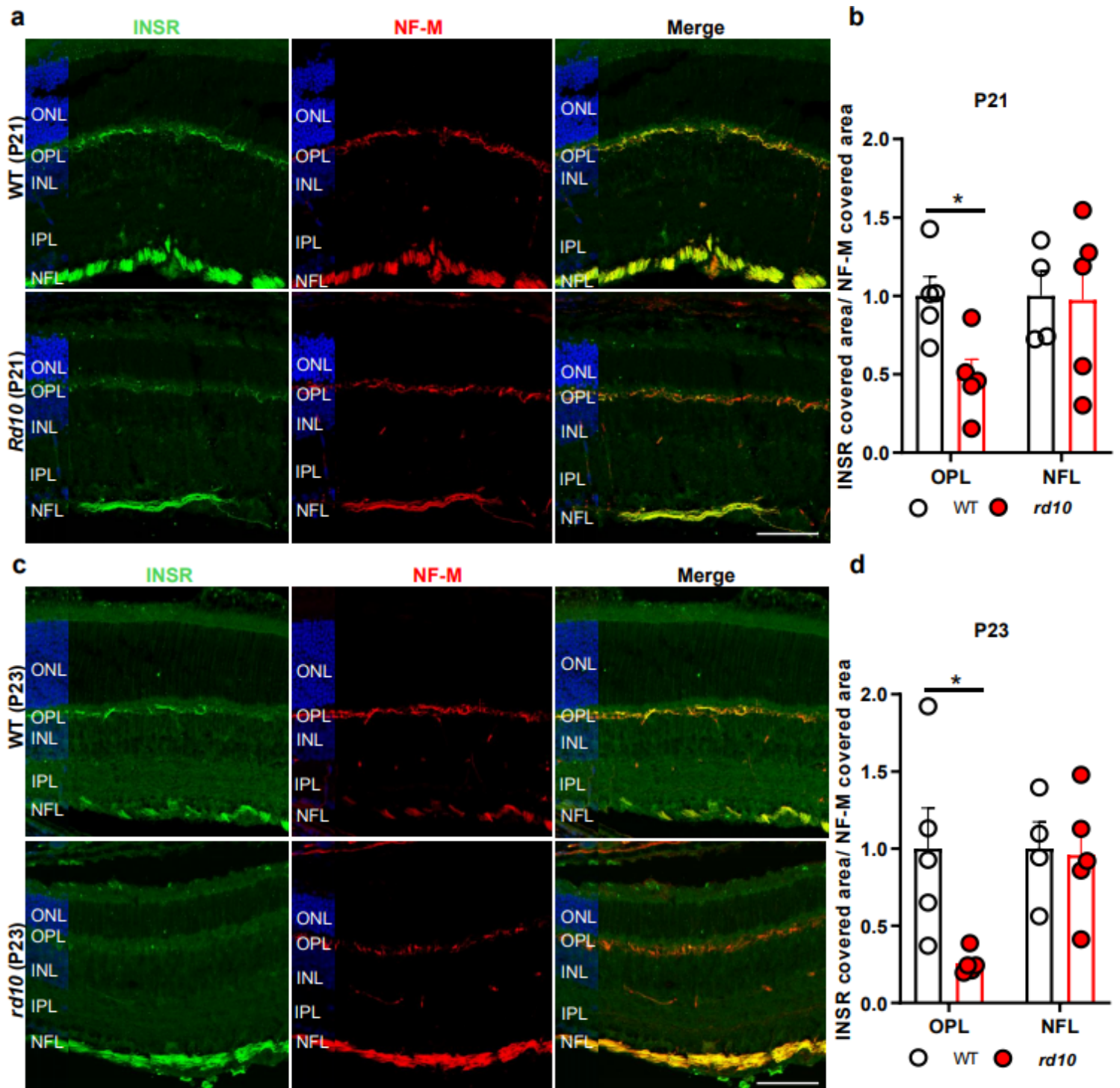


Figure 2

Downregulation of insulin receptor expression in the rd10 retina. a, c. Representative images of P21 (a) and P23 (c) retinal sections from WT and rd10 mice co-immunostained for INSR (green) and neurofilament-M (NF-M, red). Nuclei are stained with DAPI (blue). ONL, outer nuclear layer; OPL, outer plexiform layer; INL, inner nuclear layer; IPL, inner plexiform layer; NFL, nerve fiber layer. Scale bar: 66 μ m. b, d. Quantification of the area of INSR-positive staining in P21 (b) and P23 (d) WT and rd10 retinal

sections. The area corresponding to INSR immunostaining was normalized to that of neurofilament-M within the same region to correct for potential variations among retinal sections, and to INSR immunostaining in corresponding WT sections (=1.0). Data are presented as the mean + SEM. n=4-5 mice, 4 images per retina. * $p \leq 0.05$ (unpaired-T test in b and unpaired-T test with Welch's correction in d).

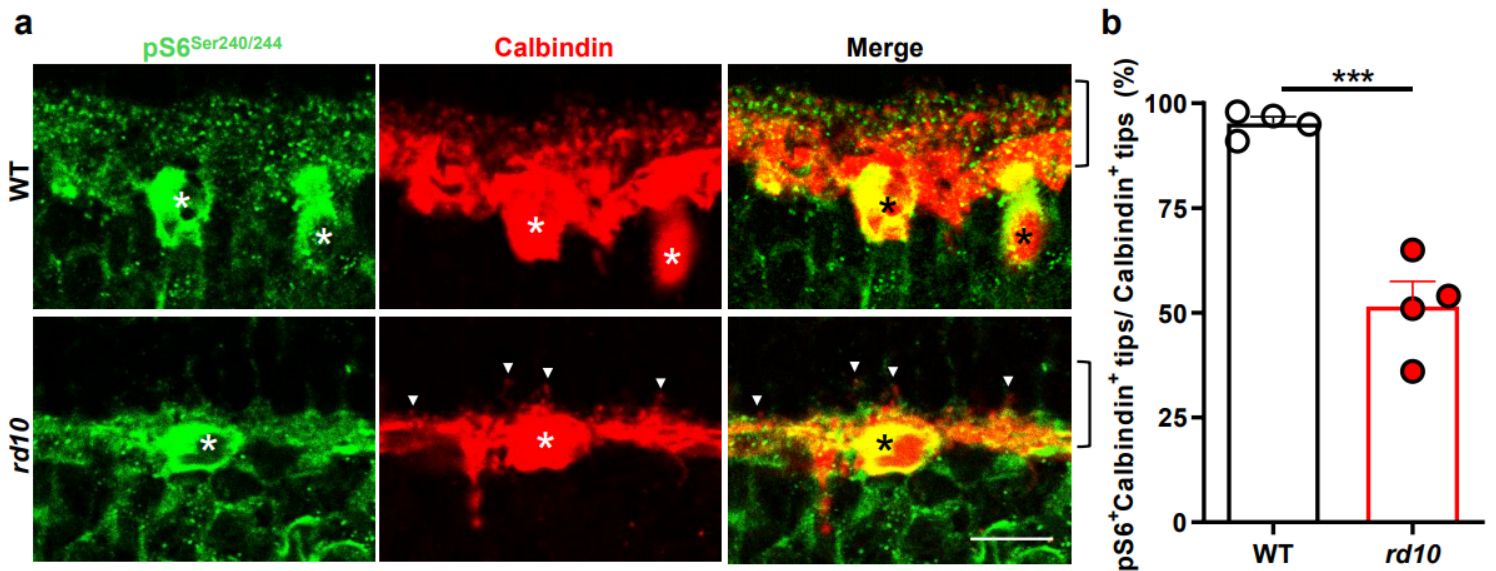


Figure 3

Downregulation of insulin receptor signaling in the rd10 retina. a. Representative images of the OPL of P23 retinal sections from WT and rd10 mice co-immunostained for pS6Ser240/244 (green) and calbindin (red). Arrows indicate horizontal cell terminal tips (calbindin+ puncta) without apposite pS6Ser240/244 labeling. Asterisks indicate horizontal cell bodies. Brackets delimit the OPL. Scale bar: 12 μ m. b. Quantification of the number of horizontal terminal tips (calbindin+ puncta) with apposite pS6Ser240/244 labeling. Data are presented as the mean + SEM. n=4 mice, 4 images. Over 200 calbindin+ tips were scored per retina. *** $p \leq 0.001$ versus WT (unpaired T-test).

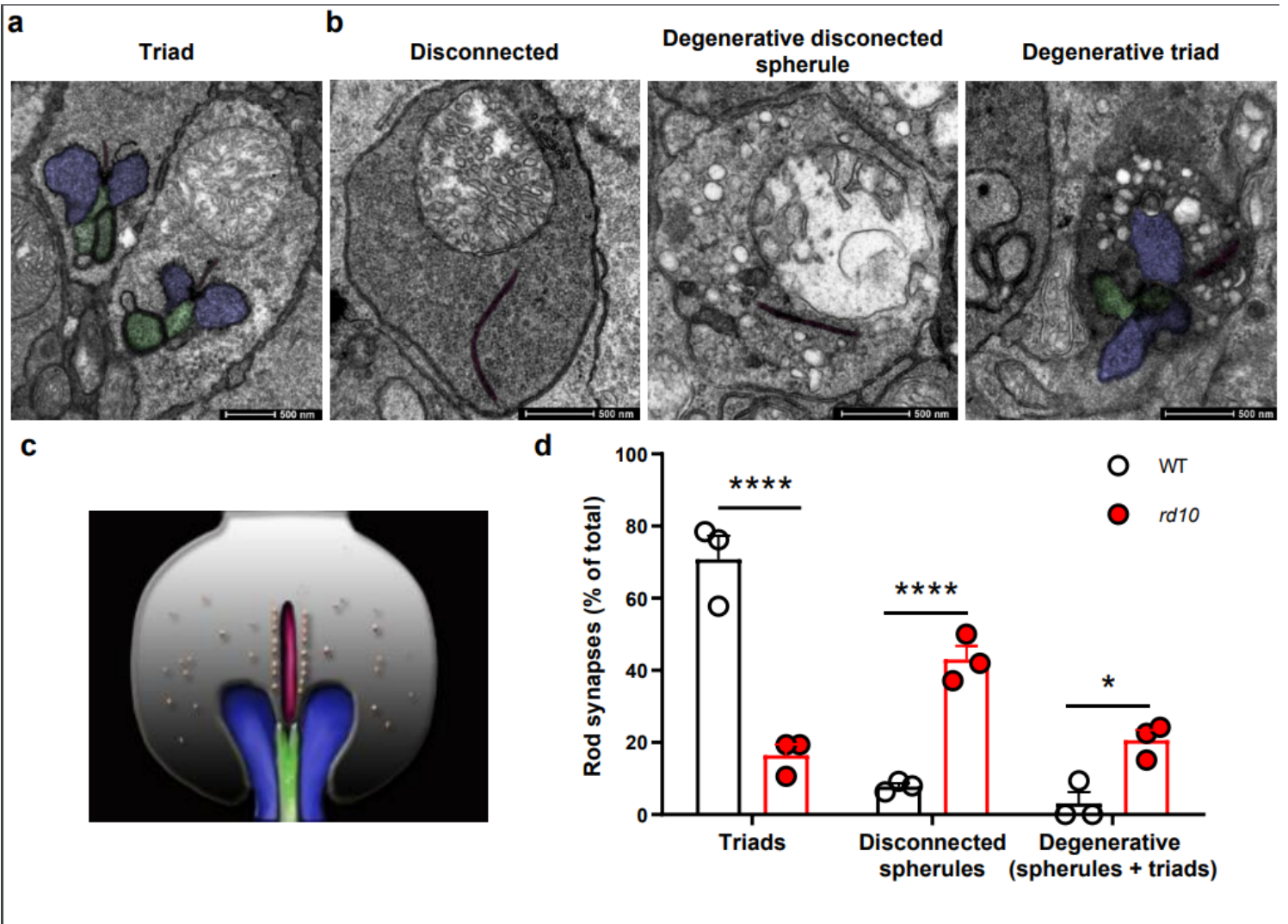


Figure 4

Ultrastructural analysis of rod photoreceptor synapses. A, b. Representative electron microscopy images of P21 WT (a) and *rd10* (b) rod synapses. Synapses were categorized as follows: Triad, rod spherule with horizontal and bipolar invaginating postsynaptic terminals; Disconnected, viable rod spherule without postsynaptic elements; Degenerative disconnected spherule, rod spherule lacking postsynaptic profiles with characteristic signs of degeneration; Degenerative triad, rod spherule containing postsynaptic profiles but showing characteristic signs of degeneration. Scale bar: 500 nm. c. Schematic diagram showing the structure of a rod triad synapse. The rod spherule (grey) consists of the synaptic ribbon (dark red) and a scaffold structure containing presynaptic vesicles (orange circles). Horizontal cell postsynaptic terminals (blue) and bipolar dendrites (green) invaginate into the rod presynaptic terminal (spherule). d. Quantification of the proportions of the different synaptic types. Results are expressed as the mean + SEM. $n=3$ mice. Over 60 synapses were scored per mouse. **** $p \leq 0.0001$, * $p \leq 0.05$ (2-way ANOVA followed by Sidak's multiple comparison test).

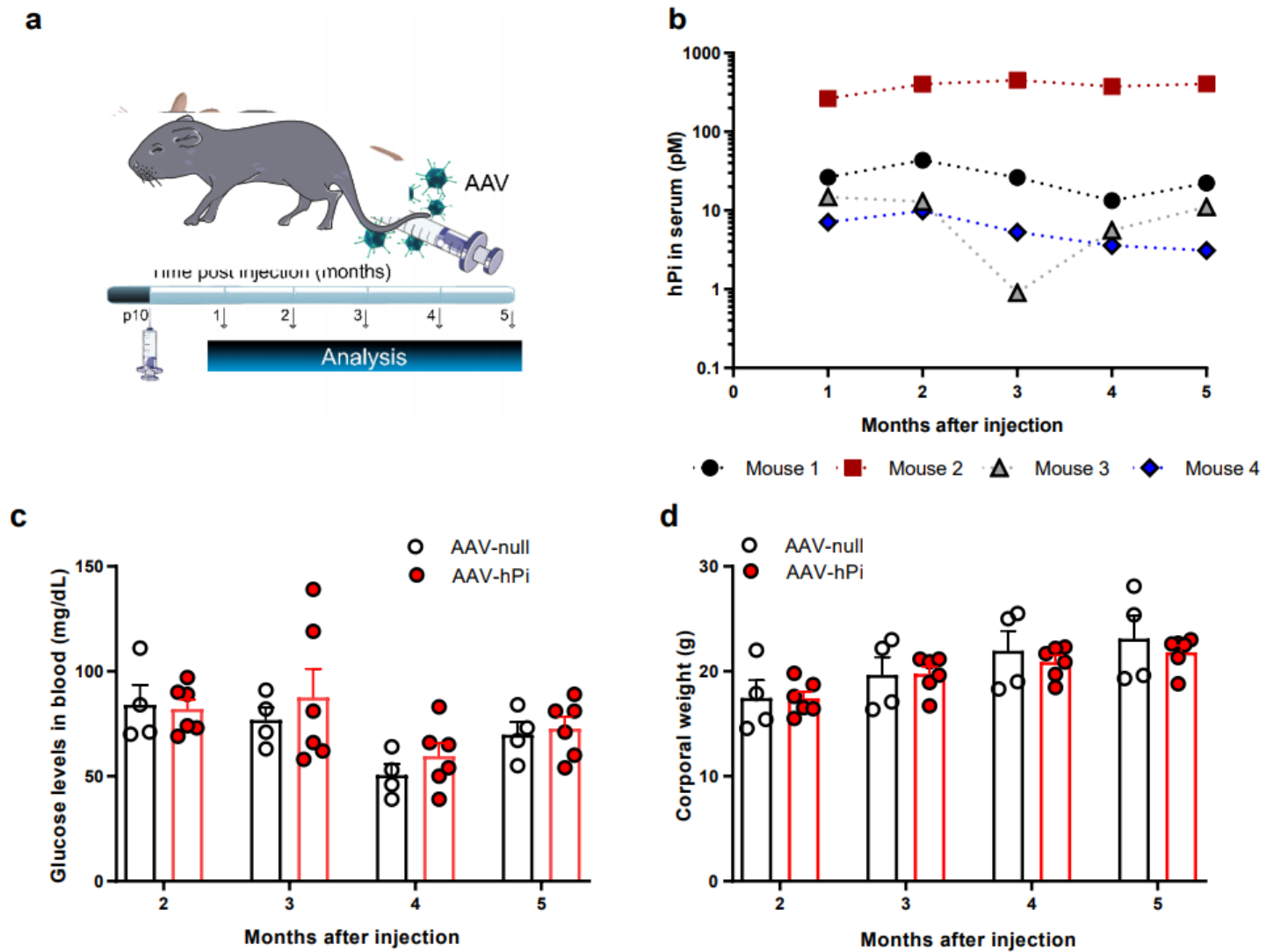


Figure 5

AAV-hPi treatment results in sustained hPi production. a. rd10 mice received a single intramuscular injection of AAV-hPi or AAV-null at P10 and were analyzed at different timepoints post-injection. b. Long-term monitoring of serum hPi levels as determined by ELISA in individual rd10 mice injected with AAV-hPi. c, d. Long-term monitoring of glucose levels (c) and body weight (d) in AAV-hPi or AAV-null injected rd10 mice. Data are presented as the mean + SEM. n=4 mice in B and 4–6 mice per group in c and d.

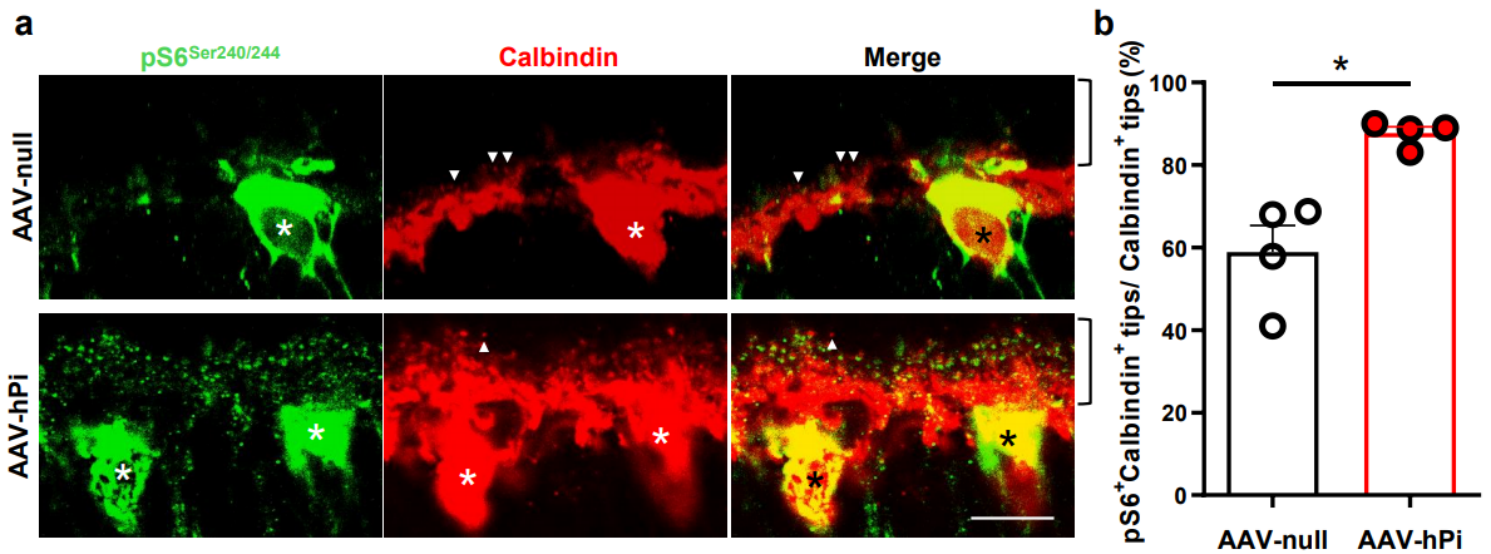


Figure 6

Effect of AAV-hPi administration on insulin receptor signaling. rd10 mice received a single intramuscular injection of AAV-null or AAV-hPi at P12 and pS6Ser240/244 expression was analyzed at P21. **a**. Representative images of the OPL in P21 retinal sections co-immunostained for pS6Ser240/244 (green) and calbindin (red). Arrows indicate horizontal cell terminal tips (calbindin+ puncta) without apposite pS6Ser240/244 labeling. Asterisks indicate horizontal cell bodies. Brackets delimit the OPL. Scale bar: 11 μ m. **b**. Quantification of the number of horizontal terminal tips (calbindin+ puncta) with apposite pS6Ser240/244 labeling. Data are presented as the mean + SEM. n=4 mice, 4 images. Over 200 calbindin+ tips per retina were analyzed. * $p \leq 0.05$ versus AAV-null (unpaired T-test with Welch's correction).

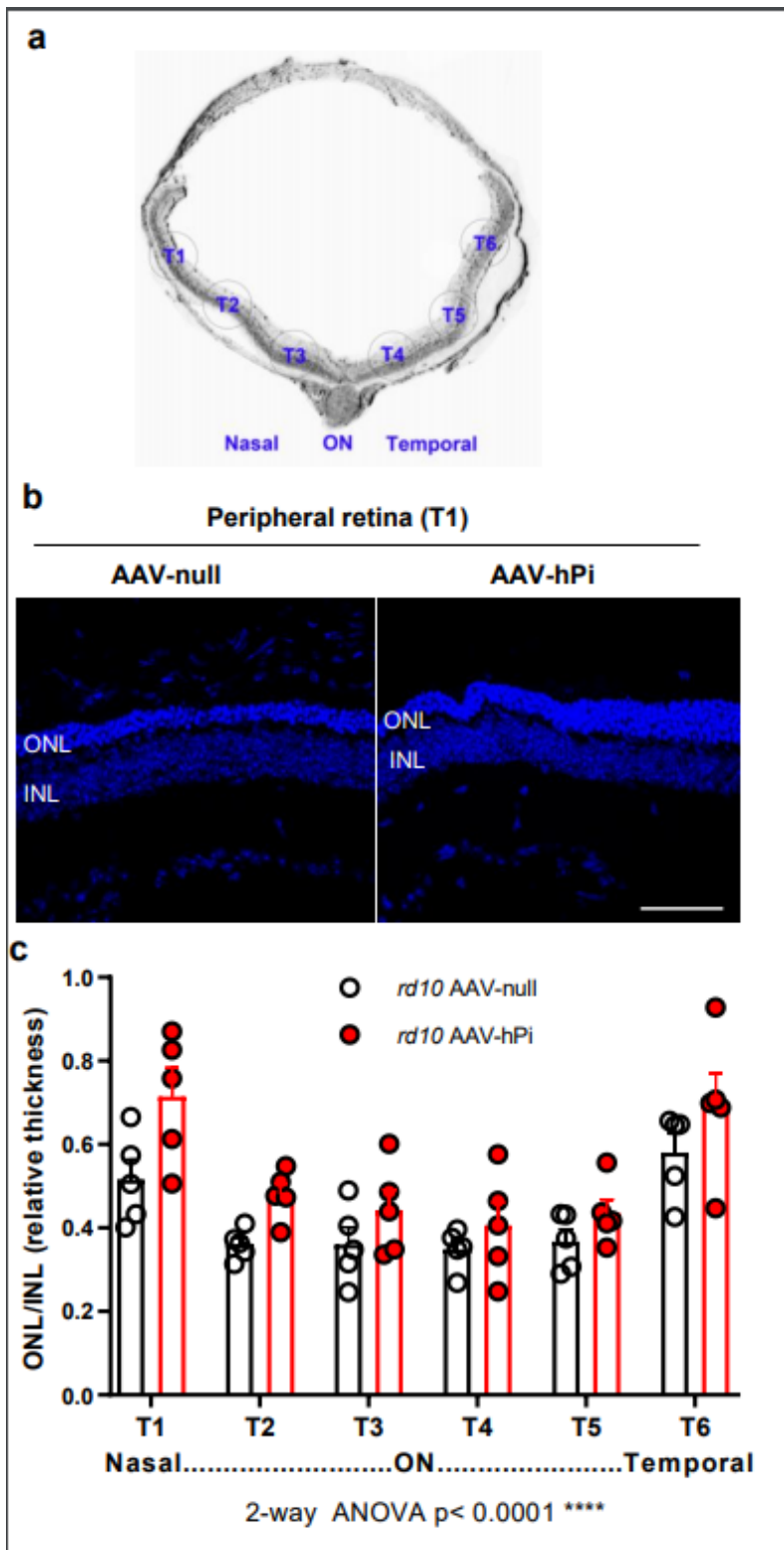


Figure 7

Effect of AAV-hPi administration on photoreceptor preservation. *rd10* mice received a single intramuscular injection of AAV-null or AAV-hPi at P12 and were analyzed at P30. a. Schematic depicting retinal sections. The 6 retinal zones in which quantification was performed (T1, T2, T3, T4, T5 and T6) are indicated. ON, optic nerve. b. Representative images of P30 retinal sections showing the T1 region from AAV-null- and AAV-hPi-treated *rd10* mice. Blue color corresponds to DAPI staining. ONL, outer nuclear

layer; INL, inner nuclear layer. Scale bar: 70 μm . c. ONL and INL thickness were measured in equatorial sections corresponding to 6 retinal areas, following a nasotemporal sequence (T1–T6 as defined in panel A). Plot shows the mean + SEM. $n=5$ mice, 3 sections per retina, 6 regions, 3 measurements per region. ON, optic nerve. **** $p \leq 0.0001$ (2-way ANOVA).

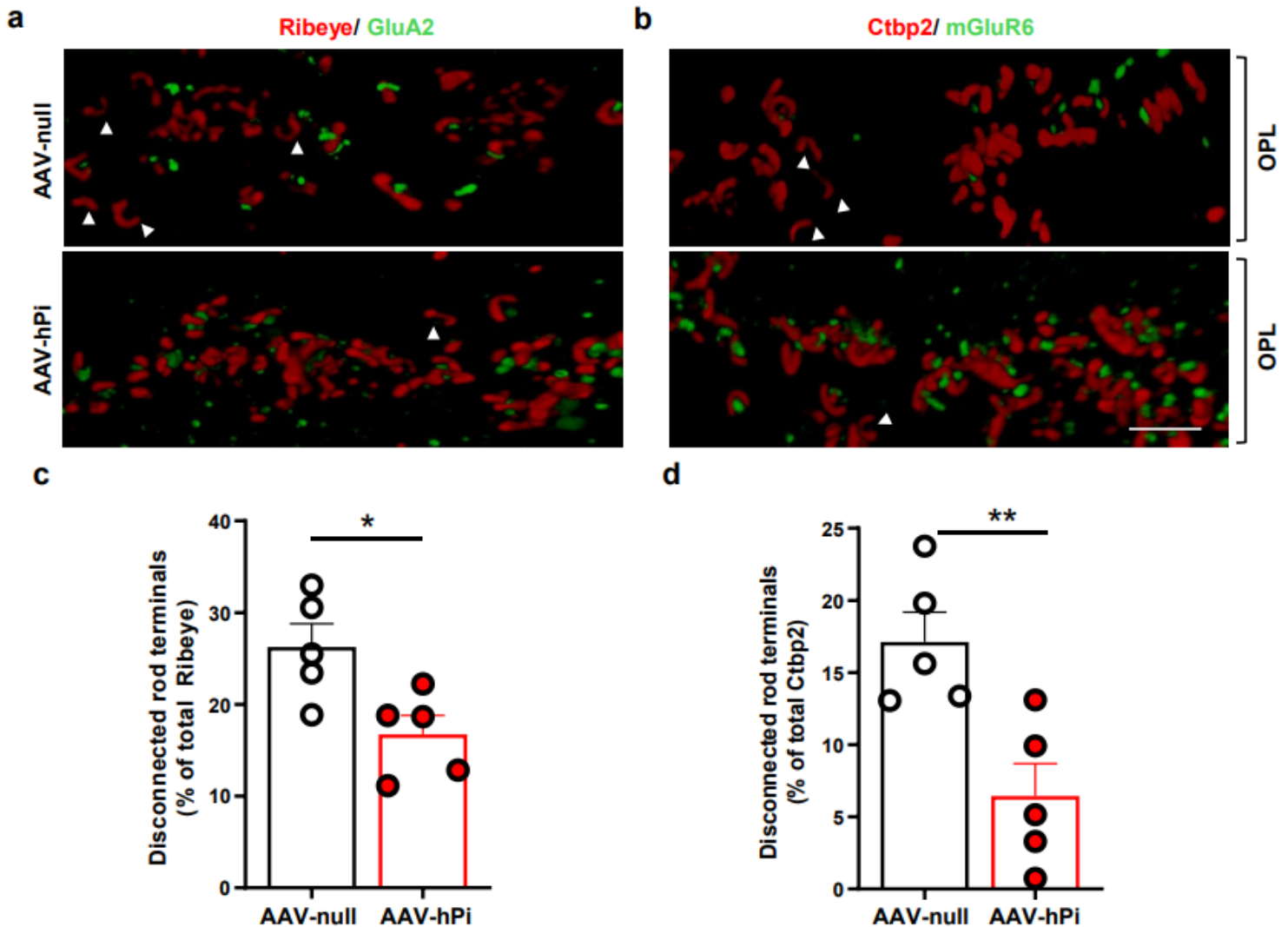


Figure 8

Effect of AAV-hPi administration on rod horizontal and rod bipolar synapses. rd10 mice received a single intramuscular injection of AAV-null or AAV-hPi at P12 and were analyzed at P30. a, b. Representative 3D reconstructions of synapses in the OPL. Retinal sections were co-immunostained for Ribeye (ribbon at presynaptic terminal, red) and the glutamate receptor subunit GluA2 (horizontal postsynaptic terminal, green) (a), or for Ctbp2 (ribbon at presynaptic terminal, red) and the glutamate receptor mGluR6 (bipolar postsynaptic terminal, green) (b). Arrowheads indicate ribbons (rod presynaptic terminals) without postsynaptic partners. OPL, outer plexiform layer. Scale bar: 3 μm . c, d. Quantification of the number of disconnected rod presynaptic terminals. Percentage of ribbons without associated GluA2 (c) or mGluR6

(d) punctate staining. Plots show the mean + SEM. n = 5 mice. Over 200 ribbons were analyzed per retina. *p ≤ 0.05 (unpaired T-test).

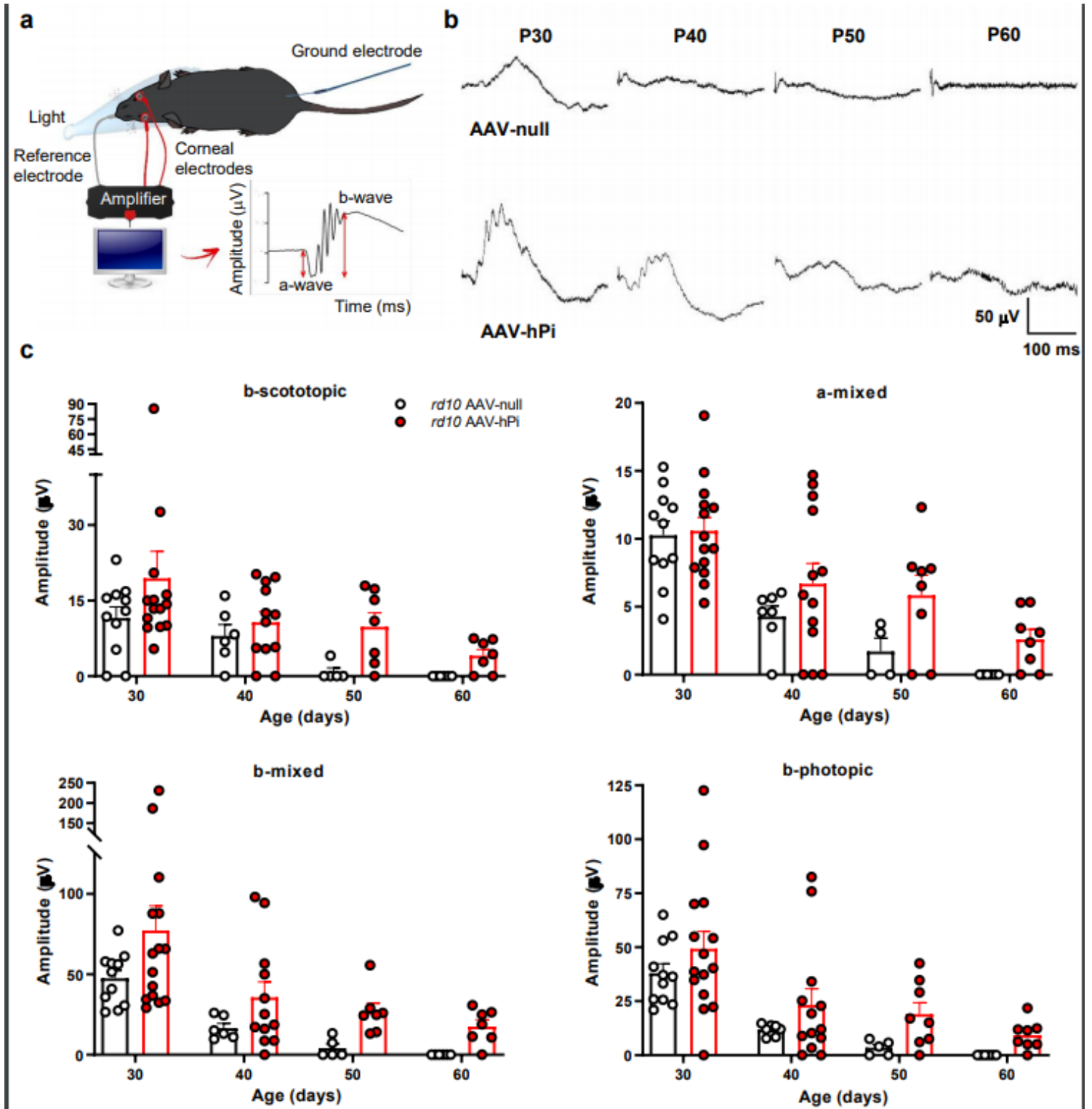


Figure 9

Effect of AAV-hPi administration on retinal response to light. *rd10* mice received a single intramuscular injection of AAV-null or AAV-hPi at P10. ERG recordings were performed at the indicated ages. a. Schematic diagram depicting the ERG recording method. b. Standard ERG representative trace recordings

of the mixed response obtained from 1 AAV-null- and 1 AAV-hPi-treated mouse over the course of the study (P30–P60) in response to a light stimulus of 1.5 cd·s/m². Note the differences in the traced amplitudes between the 2 animals. c. Graphs show averaged ERG wave amplitudes, plotted as a function of animal age. Amplitudes of the rod response (b-scotopic; light intensity = -2 log cd·s/m²) and rod and cone mixed response (a-mixed and b-mixed; light intensity = 2 log cd·s/m²) were recorded under scotopic conditions after overnight adaptation to darkness. Cone amplitudes (b-photopic; light intensity = 2 log cd·s/m²) were recorded after 5 minutes of light-adaptation (30 cd/m² background light) under photopic conditions. Results are expressed as the mean + SEM. n=4–13 mice. Significant differences between AAV-null- and AAV-hPi-treated mice were observed for b-scotopic, a-mixed, b-mixed, and b-photopic responses ($p \leq 0.05$) (2-way ANOVA).

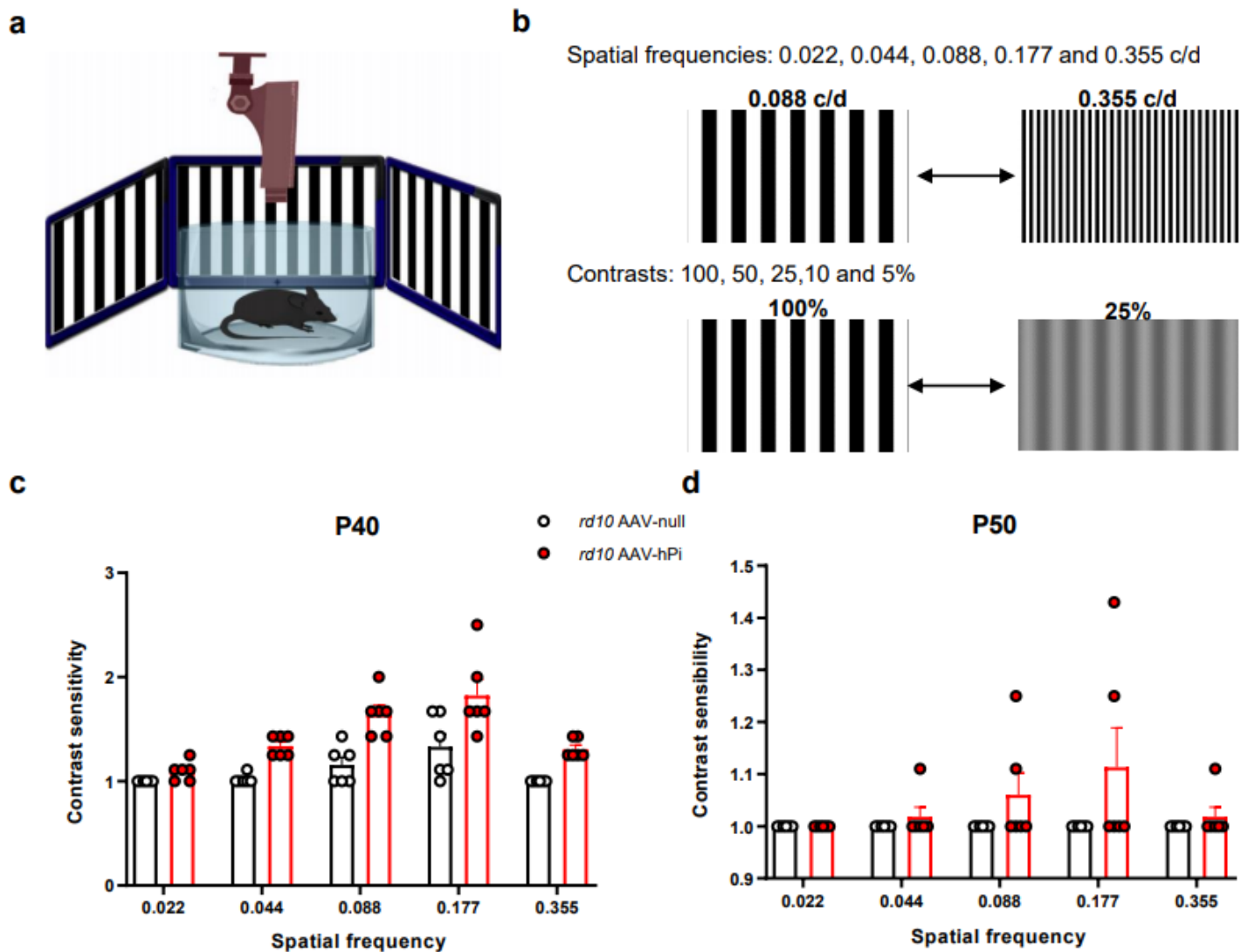


Figure 10

Effect of AAV-hPi administration on optokinetic response. *rd10* mice received a single intramuscular injection of AAV-null or AAV-hPi at P10. The optomotor test was performed at the indicated ages. a, b. Schematic depicting the optomotor test (a); 5 different spatial frequencies were tested (0.022–0.355 cycles/degree). The contrast of the moving bars was adjusted (from 100% to 5%) to determine contrast

sensitivity (b). c, d. Optokinetic responses recorded at the indicated ages in AAV-null- and AAV-hPi treated rd10 mice. Contrast sensitivity is represented as a function of spatial frequency. Data are presented as the mean + SEM. n=6 mice. Significant differences were observed between AAV-null- and AAV-hPi treated mice at P40 ($p \leq 0.05$) and P50 ($p \leq 0.0001$) (2-way ANOVA).

Supplementary Files

This is a list of supplementary files associated with this preprint. Click to download.

- [renamed3cc95.pdf](#)